



A Distant Fast Radio Burst Associated with Its Host Galaxy by the Very Large Array

Casey J. Law¹, Bryan J. Butler², J. Xavier Prochaska^{3,4}, Barak Zackay⁵, Sarah Burke-Spolaor^{6,7,8},
Alexandra Mannings³, Nicolas Tejos⁹, Alexander Josephy^{10,11}, Bridget Andersen^{10,11}, Pragma Chawla^{10,11},
Kasper E. Heintz¹², Kshitij Aggarwal⁷, Geoffrey C. Bower¹³, Paul B. Demorest², Charles D. Kilpatrick³,
T. Joseph W. Lazio¹⁴, Justin Linford², Ryan Mckinven^{15,16}, Shriharsh Tendulkar^{10,11}, and Sunil Simha³

¹ Cahill Center for Astronomy and Astrophysics, MC 249-17 California Institute of Technology, Pasadena, CA 91125, USA; claw@astro.caltech.edu

² National Radio Astronomy Observatory, Socorro, NM 87801, USA

³ University of California Observatories-Lick Observatory, University of California, 1156 High Street, Santa Cruz, CA 95064, USA

⁴ Kavli Institute for the Physics and Mathematics of the Universe, 5-1-5 Kashiwanoha, Kashiwa, 277-8583, Japan

⁵ Institute for Advanced Study, Princeton, USA

⁶ Center for Gravitational Waves and Cosmology, West Virginia University, Chestnut Ridge Research Building, Morgantown, WV 26505, USA

⁷ Department of Physics and Astronomy, West Virginia University, Morgantown, WV 26506, USA

⁸ CIFAR Azrieli Global Scholars program, CIFAR, Toronto, Canada

⁹ Instituto de Física, Pontificia Universidad Católica de Valparaíso, Casilla 4059, Valparaíso, Chile

¹⁰ Department of Physics, McGill University, 3600 University Street, Montréal, QC H3A 2T8, Canada

¹¹ McGill Space Institute, McGill University, 3550 University Street, Montréal, QC H3A 2A7, Canada

¹² Centre for Astrophysics and Cosmology, Science Institute, University of Iceland, Dunhagi 5, 107 Reykjavik, Iceland

¹³ Academia Sinica Institute of Astronomy and Astrophysics, 645 N. A'ohoku Place, Hilo, HI 96720, USA

¹⁴ Jet Propulsion Laboratory, California Institute of Technology, 4800 Oak Grove Dr, M/S 67-201, Pasadena, CA 91109 USA

¹⁵ Department of Astronomy and Astrophysics, University of Toronto, 50 St. George Street, Toronto, ON M5S 3H4, Canada

¹⁶ Dunlap Institute for Astronomy and Astrophysics, University of Toronto, 50 St. George Street, Toronto, ON M5S 3H4, Canada

Received 2020 June 5; revised 2020 July 4; accepted 2020 July 8; published 2020 August 26

Abstract

We present the discovery and subarcsecond localization of a new fast radio burst (FRB) by the Karl G. Jansky Very Large Array (VLA) and *realfast* search system. The FRB was discovered on 2019 June 14 with a dispersion measure of 959 pc cm^{-3} . This is the highest DM of any localized FRB and its measured burst fluence of 0.6 Jy ms is less than nearly all other FRBs. The source is not detected to repeat in 15 hr of VLA observing and 153 hr of CHIME/FRB observing. We describe a suite of statistical and data quality tests we used to verify the significance of the event and its localization precision. Follow-up optical/infrared photometry with Keck and Gemini associate the FRB with a pair of galaxies with $r \sim 23 \text{ mag}$. The false-alarm rate for radio transients of this significance that are associated with a host galaxy is roughly $3 \times 10^{-4} \text{ hr}^{-1}$. The two putative host galaxies have similar photometric redshifts of $z_{\text{phot}} \sim 0.6$, but different colors and stellar masses. Comparing the host distance to that implied by the dispersion measure suggests a modest ($\sim 50 \text{ pc cm}^{-3}$) electron column density associated with the FRB environment or host galaxy/galaxies.

Unified Astronomy Thesaurus concepts: [Radio transient sources \(2008\)](#); [Radio interferometry \(1346\)](#); [Extragalactic astronomy \(506\)](#); [Radio bursts \(1339\)](#)

1. Introduction

Fast radio bursts (FRBs) are millisecond-timescale radio transients of extremely high brightness originating at cosmological distances (Cordes & Chatterjee 2019; Petroff et al. 2019). Hundreds of FRBs are known currently, and the inferred occurrence rate is roughly $10^3 \text{ sky}^{-1} \text{ day}^{-1}$ above a fluence limit of 1 Jy ms at frequencies near 1.4 GHz (Champion et al. 2016; Lawrence et al. 2017). FRB distances can be estimated from the dispersive delay induced by propagation through ionized gas (quantified by a dispersion measure, DM, which measures the total electron column density along the line of sight to the source); for FRBs, the measured DMs are significantly larger than those expected due to contributions from our own Galaxy (Cordes & Lazio 2002). By attributing the dispersion induced outside of our Galaxy to predictions for the intergalactic medium (IGM), FRBs are estimated to originate at characteristic distances of one to a few gigaparsecs (Inoue 2004; Lorimer et al. 2007). Several FRBs have been localized by radio interferometers and associated with host galaxies of known distance; their luminosity distances range from 149 Mpc to 4 Gpc (Tendulkar et al. 2017; Bannister et al. 2019; Prochaska et al. 2019b; Ravi et al. 2019; Macquart et al. 2020; Marcote et al. 2020).

It is not yet known what causes FRBs or whether there are multiple formation channels (Lu & Kumar 2016; Ravi 2019a). The identification of FRB host galaxies is a critical test of formation models, as it can constrain the age of the stellar populations in FRB environments. The first host galaxy suggested that FRBs are associated with peculiar star-forming environments (Bassa et al. 2017) but later hosts have a wider range of environments (Bannister et al. 2019; Ravi et al. 2019; Bhandari et al. 2020).

Radio waves are modified as they propagate through ionized gas (e.g., dispersion, scattering, lensing, and Faraday rotation; Cordes et al. 2017; Vedantham & Ravi 2019). This fact, combined with the large distance to FRBs, makes them novel probes of the IGM and other galaxies (Ginzburg 1973; Masui et al. 2015; Prochaska et al. 2019b). Furthermore, the fact that dispersion is an unambiguous tracer of baryonic mass has revealed the potential of using FRBs to study galaxy halos and cosmology (Prochaska & Zheng 2019; Ravi 2019b). However, most of this scientific potential can only be achieved by measuring distances to FRBs. Multiple radio interferometers that can be used for precise FRB localization are in phases of conceptual development, construction, or commissioning

(Oostrum et al. 2017; Law et al. 2018; Bannister et al. 2019; Caleb et al. 2019; Kocz et al. 2019). The goal of all these projects is to localize FRBs to arcsecond precision, which is required to unambiguously associate them with a host galaxy (Eftekhari et al. 2018).

Many FRBs are seemingly single flashes, and before the advent of widespread use of GPUs to accelerate complex processing, single-dish telescopes generally led blind searches for new FRBs (Burke-Spolaor et al. 2011; Thornton et al. 2013; Spitler et al. 2014). However, some FRBs, such as FRB 121102, emit multiple bursts at irregular intervals (Spitler et al. 2016; Zhang et al. 2018), which made it possible to target them with interferometers (Chatterjee et al. 2017; Marcote et al. 2017). The Canadian Hydrogen Intensity Mapping Experiment (CHIME) is a transit telescope operating between 400 and 800 MHz that is rapidly discovering both repeating and nonrepeating FRBs (CHIME/FRB Collaboration et al. 2018; The CHIME/FRB Collaboration et al. 2019). The CHIME/FRB search has a localization precision of roughly $10'$, which is too large to unambiguously identify host galaxies for FRBs.

Here, we present a new FRB discovery and localization by the Karl G. Jansky Very Large Array (VLA) using *realfast* (Law et al. 2018). The FRB was found coincidentally during a search for CHIME/FRB FRB 180814.J0422+73 (hereafter FRB 180814, CHIME/FRB Collaboration et al. 2019). This new FRB is associated with a unique host galaxy with a distance that is consistent with expectations for its DM. The combination of radio interferometric data and optical associations support the conclusion that it is a new FRB, and we refer to it as FRB 20190614D. We discuss the FRB environment and constraints on the distribution of DM in the IGM and host galaxy.

2. Observations

2.1. Program and Overall Description

In 2018, the VLA and CHIME/FRB teams began collaborating to use the VLA for follow-up of repeating FRBs found by CHIME/FRB. We have carried out two approved projects: VLA/18B-405 and VLA/19A-331. We targeted FRB 180916.J0158+65 and FRB 190303.J1353+48 for 40 hr scheduled under VLA/18B-405 and FRB 180814 for 39 hr scheduled under VLA/19A-331; this paper focuses on the second project.

We observed using the *L*-band system of the VLA, spanning 1–2 GHz, in 20 separate observations. We observed a field centered at (R.A., decl.) [J2000] = (04^h22^m22^s, +73^d40^m00^s), the approximate position of FRB 180814. The nominal field of view of the VLA antennas at *L*-band is $\sim 30'$ (FWHM at 1.4 GHz), but the *realfast* system is configured to image a field two times wider than that. The first seven observations were performed in 2018 December, in the C-configuration of the VLA, with maximum baselines ~ 3 km and a resolution of $\sim 14''$ at 1.4 GHz. Thirteen later observations were performed in February through July of 2019, in the B- or BnA-configurations of the VLA, with maximum baselines ~ 11 km in length and a resolution of $\sim 4.5''$ at 1.4 GHz. Each observation had an on-source time of around 1.5 hr that was searched by the *realfast* system. The detection reported here is the strongest FRB-like event found in this campaign and is the focus of the analysis presented.

2.2. Search Technique

The observations used a commensal correlator mode that generated visibilities with an integration time of 5 ms to be searched by *realfast*. The same data were also used to generate and save the standard visibility data product to the NRAO archive with a sampling time of 3 s, for all observations in 2019 June and July (nine of them). Prior to that, all visibilities were saved to the archive at their full time resolution, resulting in large data sets (of order 1.5 TB). Both fast and slow visibilities were made in 16 64-channel spectral windows, with each channel set to a width of 1 MHz. Taking typical interference flagging into account, the usable bandwidth is 600 MHz.

The fast-sampled visibilities were distributed to a dedicated GPU cluster using *vysmaw* (Pokorny et al. 2018) and searched with *rfpipe* (Law 2017). After applying available online calibrations, the search pipeline dedispersed and integrated visibilities in time before forming images. Calibration solutions were derived from \sim minute-long scans and are stable in time (less than 5° change from the mean value). Images were generated with a simple, custom algorithm that uses natural weighting and a pillbox gridding scheme. The search used 215 DM values from 0 to 1000 pc cm⁻³ and four temporal widths from 5 to 40 ms, which is inclusive of the known properties of FRB 180814 (CHIME/FRB Collaboration et al. 2019).

For the B-configuration observations, each image had 2048×2048 pixels with a pixel size of $1''.7$, covering a field of view of 1° . The C-configuration images were 512×512 pixels with a pixel size of roughly $6''.8$. The nominal 1σ sensitivity in a single 5 ms integration is 6 mJy beam⁻¹. All candidates detected with significance greater than 7.5σ trigger the recording of 2–3 s of fast-sampled visibilities and a visualization of the candidate. Each candidate is classified by *fetch*, a convolutional neural network for radio transients (Agarwal et al. 2020). Finally, *realfast* team members review the visualizations of the real-time analysis to either remove data corrupted by interference or identify candidates for more refined offline analysis.

2.3. Discovery

On 2019 June 14 (UT), the *realfast* system detected a candidate transient in the FRB 180814 field. The real-time detection system reported a candidate with image significance of 8.0σ and DM = 959 pc cm⁻³, far in excess of the expected DM contribution of the Milky Way (83.5 pc cm⁻³; Cordes & Lazio 2002). However, the DM of FRB 180814 is 189.4 pc cm⁻³; no FRB has shown changes in DM of more than a few pc cm⁻³ (Gajjar et al. 2018), so the candidate FRB is likely unrelated to the CHIME FRB.

The real-time candidate analysis revealed multiple signatures consistent with an astrophysical source. First, the spectrum (Figure 1, right panel) shows emission over a range of frequencies spanning at least 50 MHz and the image shows a compact source. Most sources of interference tend to have circular polarization, narrow spectral extent, or are spatially incoherent (i.e., radio frequency interference in the near-field of the array). Second, the *fetch* FRB classification system reported an astrophysical probability of 99.9%. Third, there is a weak prior expectation for blindly detected astrophysical events to be detected where the antenna sensitivity is highest. The candidate was detected roughly $9'$ away from the pointing

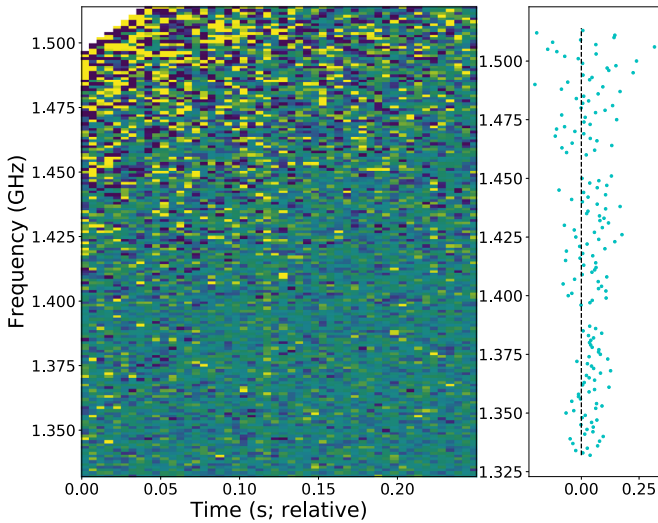


Figure 1. (Left) Stokes I dynamic spectrum for the candidate FRB as seen by VLA/*realfast*. The dynamic spectrum was generated by summing calibrated visibilities for all baselines and the two orthogonal polarizations. The gap and higher noise level toward the top left of the dynamic spectrum results from when the data recording was initiated. (Right) Stokes I spectrum taken from a single 5 ms integration of the dynamic spectrum.

center, where the antenna has roughly 80% of its nominal sensitivity; only 10% of the image has this sensitivity or higher.

The *realfast* search system was starting to receive visibilities from the VLA correlator during the burst. This is seen in Figure 1, which shows that the mean of all recorded visibilities during the burst (phased toward the event) is noisier at early times and at higher frequencies. Visibilities for each baseline, polarization, and spectral window (64 channels) are distributed separately such that the fraction of data grows to 100% over a few hundred milliseconds as the system turns on.

2.4. Verification Tests and Significance Analysis

Traditional fast transient surveys measure event significance based on a noise estimate that is local in time (e.g., a standard deviation of a time series). Our interferometric search measures significance in a single image, so the noise estimate is made simultaneously. The Appendix describes how the visibility domain search can be thought of as a time-domain search that allows for more accurate noise estimates.

In our initial analysis of the candidate, we confirmed that the event significance was not affected by different flagging algorithms or calibration solutions from a calibrator observation a few minutes after the event. We also confirmed that removing an antenna from the 27-antenna array reduced the detection significance by roughly 5% ($\approx 1/27$ antennas). With confidence in the quality of data, we proceeded to more carefully quantify the event significance.

We used the raw, saved visibilities to rerun the search with a larger image (8192×8192 pixels) and finer DM grid. This optimized search improved the detection significance slightly to a signal-to-noise ratio (S/N) of 8.27 at $\text{DM} = 959.19 \text{ pc cm}^{-3}$. Using the same refinement procedure on other candidates typically does not reproduce the initial detection. Noise-like events are expected to be sensitive to the image gridding parameters, so we ignore all events that cannot be reproduced in larger images. We use these refined properties for visualizations and all further analysis.

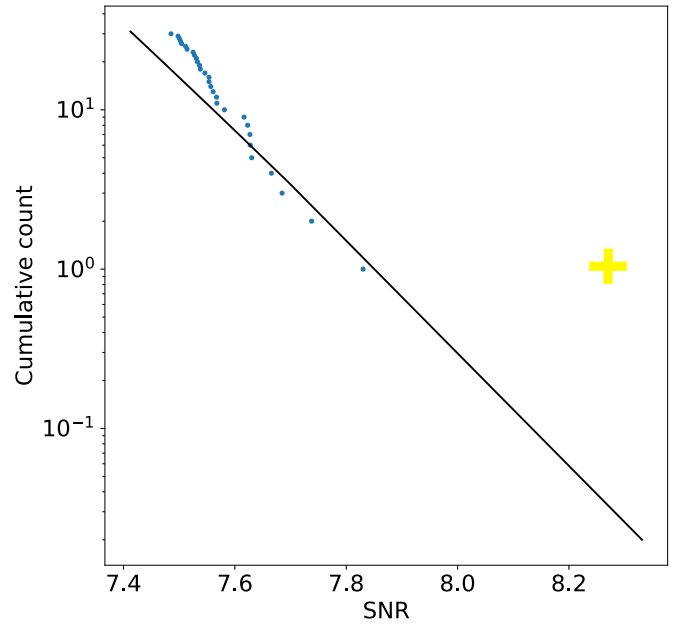


Figure 2. Circles show the cumulative distribution of candidates in this observing campaign as a function of image S/N ratio. The solid line shows the expected cumulative event rate for a Gaussian (noise-like) S/N distribution. The yellow cross shows the candidate FRB S/N ratio after refinement analysis.

Figure 2 shows the cumulative distribution of event significance for all events seen in this campaign. The FRB search pipeline automatically applies flags for bad calibration, antenna state, missing data, and interference. We visually inspected the 263 candidates detected above 7.5σ in observations of this field and removed those affected by unflagged interference to get a sample of 31 candidates.

Figure 2 also shows an independent estimate of the ideal event rate significance distribution for the array and correlator configuration used to find this candidate. The ideal cumulative event rate assumes that each pixel imaged has a brightness that is drawn from a stationary Gaussian distribution. The number of independent pixels searched is $(N_{\text{pix}}/O_{\text{pix}})^2 \times N_{\text{int}} * (N_{\text{DM}}/O_{\text{DM}})$, where N_{pix} is the width of an image in pixels, N_{int} number of integrations (at all time widths), N_{DM} is the number of DM trials, and $O_{\text{pix}/\text{DM}}$ are the oversampling of the synthesized beam and dispersion sensitivity function, respectively. Both images and DMs are oversampled to maintain uniform sensitivity to all locations and DMs. The search we run here uses $O_{\text{pix}} = 2.5$ and $O_{\text{DM}} = 3$. In this configuration, we have 8.4 hr of observing time and 5×10^{14} independent pixels. The candidate S/N of 8.27 corresponds to a false-alarm rate (FAR) of once in 250 hr. The measured and ideal distributions are independent and in rough agreement, which shows that the significance distribution approximately follows a Gaussian distribution and that this candidate is an outlier.

The FRB search pipeline also uses spectral brightness fluctuations to distinguish candidate events from noise (Law et al. 2017; The CHIME/FRB Collaboration et al. 2019). The Kalman detector (B. Zackay 2020, in preparation) is a method to estimate the statistical significance of FRB spectral variations for an assumed noise model and signal smoothness. For a given noise and signal model, we can marginalize the detection statistic over all matched filters, weighted by their prior probability. This prior probability is defined by a random walk with one free parameter, the coherence bandwidth. We calculated the Kalman score on the candidate FRB, using logarithmic spaced options

for the smoothing scale, but found no significant change in the total confidence for the candidate FRB (other FRBs do show some improvement; B. Zackay 2020, in preparation). We conclude that the candidate FRB spectrum is consistent with a constant flux density.

2.5. Localization

The real-time FRB search software makes several assumptions to improve computational efficiency, and as a result images that are used within it are not optimal. To address this, we used the stored raw, dedispersed visibilities to reimage the burst data with a combination of CASA (McMullin et al. 2007) and AIPS (Greisen 2003).¹⁷ Here, we describe a unified calibration and imaging procedure used in both fast and deep imaging. This procedure allows us to quantify the systematic error in the FRB localization.

Prior to reimagining the burst data, we reduced all of the data taken in 2019 June and July for a deep image of the field. Nine data sets during B configuration were included in this analysis. We excluded C configuration data, as it has poorer spatial resolution. We also excluded early B configuration data recorded at the fast sampling rate, as it was computationally expensive to include in the deep imaging analysis.

We started by applying the calibration and flagging tables for each observation, which were provided by the VLA calibration pipeline. For all observations, the flux density scale was set with an observation of the calibrator source 3C 147, and at these frequencies is accurate to 1%–2% (Perley & Butler 2017). Bandpass and delay calibrations were also determined by the 3C 147 observation. Complex gain (amplitude and phase) fluctuations over time were calibrated with observations of the calibrator source J0410+7656 every 30 minutes. We then exported the calibrated visibilities from CASA and imported them into AIPS. After further RFI flagging, we averaged in time (to 9 s) and frequency (to 4 MHz channels) to reduce the computational load for the imaging.

We used faceted imaging in AIPS to image beyond the first null of the antenna primary beam response (1.1° width). A total of 73 separate fields, each 1024×1024 pixels (with $0.5''$ pixel size), and 250 CLEAN boxes were used to image and clean the area. After cleaning, the 73 images of the fields were combined together, and that result was used to self-calibrate (Cornwell & Fomalont 1999) the visibilities on a 1 minute timescale. The imaging and self-calibration were then repeated using this self-calibrated data set, on a 9 s timescale—essentially self-calibrating every visibility. A final image was then made, and a primary beam correction performed on it, based on Perley (2016). This is the final deep image used for further analysis. The synthesized beam in this final deep image is $3.6'' \times 2.8''$ at a position angle of 79° (north through east). The image has a 1σ sensitivity of $3.6 \mu\text{Jy beam}^{-1}$, consistent with expectations for the total on-source time and flagging.

For the reimagining of the burst data, we first copied the VLA calibration pipeline tables (calibration and flagging) from the full June 14th observation, and ran a modified version of the procedure to reapply these tables. Calibration tables from the three spectral windows (384 MHz of bandwidth) with valid, uncorrupted data were applied. The synthesized beam in this final burst image is $10.3'' \times 4.2''$ at a position angle of 67° . It is

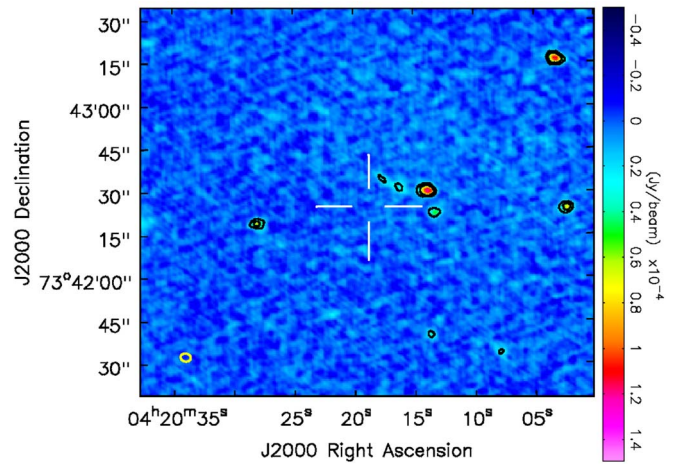


Figure 3. Deep 1.4 GHz radio image of the FRB 180814 field with the location of FRB 20190614D shown with white cross-hairs. Black contours show radio brightness levels of 25 and 50 μJy . No persistent radio emission brighter than 3σ (11 μJy) is seen at the location of the new FRB. The noise level of this image is $3.6 \mu\text{Jy beam}^{-1}$, and the beam shape is ($3.6''$, $2.8''$, 78°), marked by a yellow ellipse in the bottom left corner of the image.

Table 1
Measured Properties of FRB 20190614D with 1σ Errors

| | |
|--|---|
| Time (MJD, @2.0 GHz) | 58648.05071771 |
| R.A. (J2000) | $4^{\text{h}}20^{\text{m}}18^{\text{s}}.13$ |
| Decl. (J2000) | $+73^{\circ}42^{\text{m}}24^{\text{s}}.3$ |
| R.A. (J2000, deg) | 65.07552 |
| Decl. (J2000, deg) | 73.70674 |
| Centroid ellipse ($''$, $''$, $^\circ$) | 0.8 , 0.4 , 67 |
| S/N ratio _{image} | 8.27 |
| DM_{obs} (pc cm^{-3}) | 959.2 ± 5 |
| DM_{MW} (pc cm^{-3}) | 83.5 |
| Peak flux density (mJy) | 124 ± 14 |
| Fluence (Jy ms) | 0.62 ± 0.07 |
| Deep limit ($\mu\text{Jy beam}^{-1}$) | <11 |

Note. The centroid ellipse is defined with the major and minor axes and orientation (east of north). Deep limit refers to the flux density limit on 1.4 GHz radio counterparts in a deep image of the FRB field. The Milky Way DM estimate is calculated from Cordes & Lazio (2002).

significantly worse than the resolution of the deep image because of the drastically reduced amount of data that went into it.

The deep and fast radio images were exported to CASA format for source detection and modeling. The source detected by the *realfast* system (using *rfpipe*) is also detected in the burst image. We fit an ellipse to that source to measure the centroid location, peak flux density, and their 1σ uncertainties (see Table 1). The localization precision is approximately 1/10th of the synthesized beam diameter, which is typical for sources of this significance observed with the VLA (Becker et al. 1995).

We then searched the deep image to determine whether there is persistent radio emission associated with the candidate FRB. We find no such associated persistent radio emission at the location of the candidate FRB, to a 3σ limit of 11 μJy (see Figure 3).

We tested the astrometric precision by associating compact radio sources with optical sources in the Pan-STARRS DR2 catalog (Chambers et al. 2016). We ran the *aegean* source

¹⁷ Both CASA and AIPS calibrate with a different algorithm from that used by the real-time calibration system known as “telcal” (Law et al. 2018).

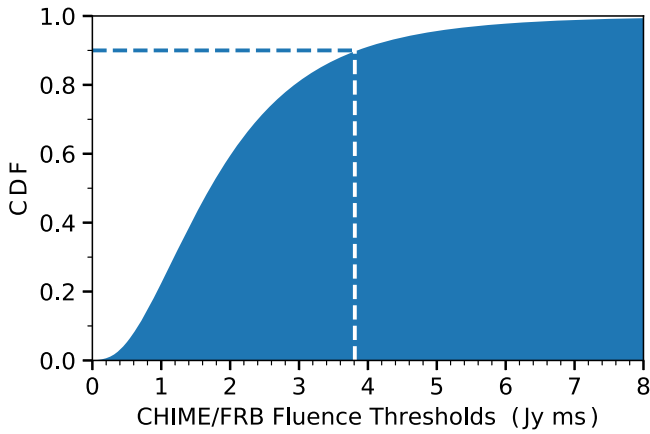


Figure 4. Cumulative distribution of fluence detection thresholds for the CHIME/FRB instrument. Note that the FRB candidate is circumpolar and thus transits the CHIME field of view twice a day; thresholds shown here are valid for the upper transit, whereas the lower transit is a factor of ~ 4 less sensitive. Dashed lines indicate the 90% completeness level at 3.8 Jy ms. For comparison, the VLA fluence limit is 0.5 Jy ms (8σ in 5 ms at 1.4 GHz).

finding package (Hancock et al. 2018) and identified 270 compact radio sources with a flux density greater than $100 \mu\text{Jy}$ ($>25\sigma$). Of these, 102 had optical counterparts within $3''$ and $n\text{Detections} = 5$. No systematic offset is found between the radio and optical sources; the standard deviation of the radio/optical offsets is $0''.2$. We note that given the resolution of the radio image ($3''.6 \times 2''.8$), we expect the astrometric accuracy to be of the order of $0''.1$ for these brighter sources (a few percent of the synthesized beamwidth).

2.6. CHIME/FRB Limits

The CHIME/FRB system, operating in its commissioning phase, has observed the sky position of FRB 20190614D for a total of 153 hr during the interval from 2018 August 28 to 2019 September 30. The large exposure is due to the circumpolar nature of the source and is split between 88 hr for the upper transit and 65 hr for the lower transit. The average duration of the upper and lower transits is 17 and 13 minutes, respectively, during which the source is within the FWHM region of the synthesized beams at 600 MHz. We searched through all low-significance events that were detected by the CHIME/FRB system in the abovementioned observing time. No significant event or excess event rate was found to be consistent with the location and DM of FRB 20190614D, so there is no evidence for repetition from this FRB.

To determine CHIME/FRB sensitivity to FRB 20190614D, we follow the methods detailed in Josephy et al. (2019). The sensitivity of CHIME/FRB varies with observing epoch, position along transit, and burst spectral shape. We used a Monte Carlo simulation with 10^6 realizations to generate fluence thresholds for different detection scenarios within the quoted exposure. These simulations define a set of relative sensitivities, which are tied to a flux density scale using beam-formed, bandpass-corrected observations. As a reference, we use a burst from FRB 180814.J0422+73 detected on 2018 November 11 with an S/N ratio of 9.8σ , fluence of 2.3 ± 0.8 Jy ms, and a Gaussian spectral fit with center frequency of 524 MHz and FWHM of 72 MHz. Figure 4 shows the fluence threshold distribution is 90% complete at 3.8 Jy ms. The distribution is valid for the upper, more-sensitive transit; we estimate the lower

transit to be approximately a factor of 4 less sensitive (CHIME/FRB Collaboration et al. 2019).

2.7. Optical Associations

We considered the significance of this candidate high enough to trigger observations designed to find an optical counterpart. On UT 2019 July 2, we observed the field surrounding FRB 20190614D with the Gemini Multi-Object Spectrograph (GMOS) on the Gemini-N telescope. We obtained a series of 8×300 s image exposures in the r -band. These data were reduced with standard procedures using the Gemini’s PYRAF package, and the images were registered using Pan-STARRS DR1 astrometric standards (Flewelling et al. 2016). We performed photometry on these images using DoPhot (Schechter et al. 1993) and calibrated the image using Pan-STARRS r -band calibrators.

On UT 2019 September 25, we obtained a series of 4×600 s images with the Low Resolution Imaging Spectrograph (LRIS) on the Keck I telescope in V and I bands. These data were reduced using a custom-built pipeline used for transient searches and based on the photpipe imaging and reduction package (Rest et al. 2005). Following standard procedures, we removed bias and flattened our images using bias and dome flat-field exposures obtained on the same night and in the same instrumental configuration. We registered the images using Pan-STARRS astrometric standards and combined the individual exposures with SWarp (Bertin et al. 2002). We performed point-spread function photometry on the final stacked images with DoPhot and calibrated these data using Pan-STARRS *grizy* calibrators transformed to VI using the bandpass transformations described in Tonry et al. (2012).

On UT 2019 November 26, we obtained an additional set of 18×200 s z -band images of the FRB field with the Alhambra Faint Object Spectrograph and Camera on the Nordic Optical Telescope (NOT). The images were processed with standard procedures and astrometrically calibrated to the Gaia-DR2 reference frame.

On UT 2020 March 9, we also obtained a set of 4×300 s images (each one coming from 5×60 s co-adds) in the near-infrared J -band using the Near InfraRed Imager and spectrograph (NIRI; Hodapp et al. 2003) on the Gemini-N telescope. The images were reduced with standard procedures using the DRAGONS¹⁸ package and were astrometrically calibrated to the Gaia-DR2 reference frame. A photometric calibration was derived using Two Micron All Sky Survey sources in the image.

Figure 5 shows the VrI images centered on the radio localization of the candidate FRB. All optical images were registered in the Pan-STARRS DR1 astrometric frame, and so the uncertainty in their relative alignment is given by the precision of the original alignment solutions. We estimate a registration precision of $\approx 0''.06$ (1σ) for each image.

There are two optical sources that are plausibly associated with the radio source. The brighter source is J042017.85+734222.8, referred to as Source A, and approximately $1''$ north of that is J042017.86+734224.5, referred to as source B. The 1σ radio localization region overlaps with source B, but the 2σ (90% confidence interval) radio localization region overlaps with source A. We consider both sources to be potentially associated with the event. Final $VrIzJ$ photometry of

¹⁸ <https://dragons.readthedocs.io>

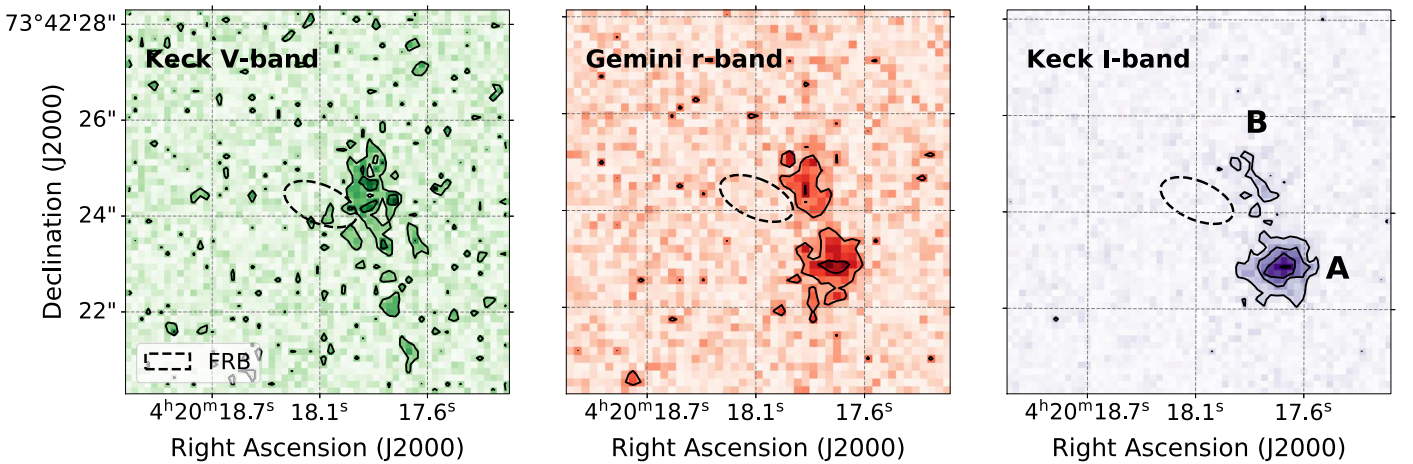


Figure 5. Cut-out images from Keck/LRIS and Gemini/GMOS centered on the candidate FRB. The dashed line shows the 1σ radio centroid region. Source A (brighter, to south) is red with brightest flux in the I band. Source B (fainter, to north) is bluer with colors indicative of star formation.

the candidate FRB hosts was obtained using a $1''$ aperture centered at the locations described in Table 2 and corrected for Galactic extinction.

With the photometry of the galaxies as inputs, we have used the software package EAZY (Brammer et al. 2008) to estimate photometric redshifts for the two sources closest to FRB 20190614D. We find $z_{\text{phot}} = 0.63 \pm 0.12$ (68% confidence interval) for source A, and $z_{\text{phot}} = 0.60 \pm 0.17$ (68% confidence interval) for source B. Figure 6 shows the redshift posterior distributions for sources A and B and their best-fitting templates. The best-fitting template for source A is a relatively quiescent galaxy with weak emission features whereas source B, which exhibits a bluer color, is best fit with a star-forming template. The spectral energy distribution (SED) templates that were fitted to the data, agree well with the color difference that we observe in the source. Testing multiple sets of SED templates, we consistently find source A to be quiescent, and similar in shape to what is shown above, as well as source B consistently being fit to star-forming, bluer templates. We also note that the $u - r$ rest-frame colors from the CIGALE analysis detailed below, are consistent with the EAZY outputs.

On UT 2019 September 29, we obtained a series of long-slit spectra ($1''$ wide) of sources A and B with LRIS configured to cover wavelengths $\lambda \approx 3200\text{--}6800\text{\AA}$ with the blue camera and its 300/5000 grism and $\lambda \approx 6720\text{--}9090\text{\AA}$ with the red camera using the 831/8200 grating. These data were reduced and calibrated with the PYPEIT software package (Prochaska et al. 2019a). While we detect a very faint trace of continuum emission from source A, there is no obvious emission or absorption feature to establish a spectroscopic redshift. This is consistent with it being an early-type galaxy with low or negligible star formation and correspondingly weak nebular emission. We did not identify any significant flux from source B.

To roughly estimate the stellar mass and rest-frame color of each candidate host galaxy, we performed an SED analysis of the measured photometry (Table 2). This analysis, using the CIGALE software package (Noll et al. 2009), also requires the source redshift; we adopted the posterior-weighted photometric redshift from the EAZY analysis (Table 2). For the SEDs constructed by CIGALE, we adopt a delayed-exponential star formation history model with no late burst population, a Chabrier initial mass function, and the Calzetti et al. (2000)

Table 2
Optical Candidates

| Quantity | Unit | Source A | | Source B | |
|-------------------|-------------|----------|---------|----------|--------|
| | | Value | Error | Value | Error |
| R.A. (J2000) | deg | 65.07380 | 0.00005 | 65.0745 | 0.0001 |
| Decl. (J2000) | deg | 73.70636 | 0.00005 | 73.7068 | 0.0001 |
| V | mag | 25.42 | 0.25 | 24.58 | 0.16 |
| r | mag | 23.25 | 0.15 | 23.94 | 0.24 |
| I | mag | 22.83 | 0.10 | 23.74 | 0.18 |
| z | mag | 23.18 | 0.30 | 22.53 | 999. |
| J | mag | 22.56 | 0.20 | 23.66 | 999. |
| z_{phot} | | 0.63 | 0.12 | 0.60 | 0.17 |
| $\log_{10} M_*$ | M_{\odot} | 9.6 | | 8.8 | |
| $u - r$ | mag | 2.1 | | 0.8 | |

Note. This AB photometry has been corrected for Galactic extinction. A 999.9 value for photometric error indicates a 3σ upper limit. Estimates for M_* and $u - r$ are based on the photometric redshift and bear great uncertainty.

dust extinction model. Because of the applied extinction corrections, changes in these assumptions would produce similar results. Consistent with the EAZY analysis, the best-fitting SEDs were quiescent for source A and star-forming for source B. In Table 2, we report estimates for the stellar mass and rest-frame $u - r$ color with the latter reflective of the inferred star-forming properties of each galaxy. We caution that the stellar mass, especially, bears great uncertainty due to the uncertain redshifts of each source.

3. Discussion

3.1. Joint Probability of Radio Candidate with Optical Association

The chance of randomly associating a point on the sky with a galaxy has previously been studied in the context of gamma-ray bursts. The chance association has an empirically defined functional form parameterized by an association between tolerance and survey depth (Bloom et al. 2002).¹⁹ Following the same approach we estimate chance association probabilities

¹⁹ Equations (1)–(3) of Bloom et al. (2002) are implemented in <https://github.com/FRBs/FRB>.

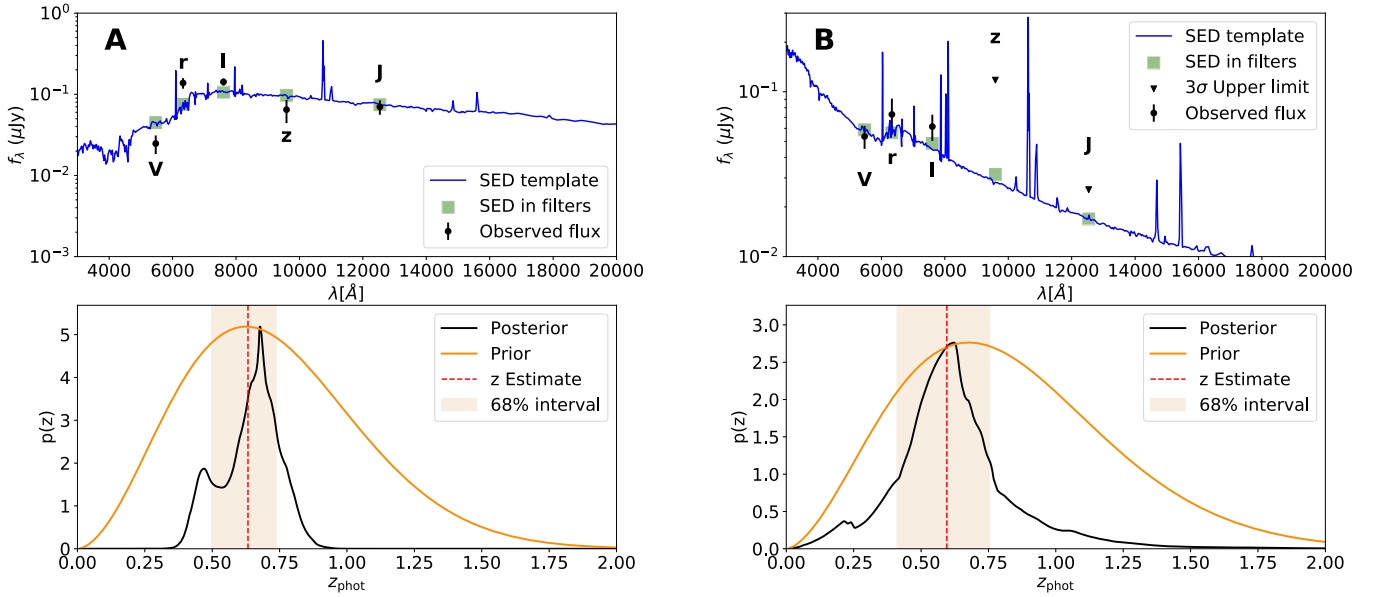


Figure 6. (Top left) The photometric measurements of source A with best-fit model in blue. SED in filters shows the best-fit template fluxes in each filter, with the black points showing the measured flux in the filters. (Bottom left) The redshift posterior for source A as estimated by EAZY. The red dashed line shows the expectation value of the redshift over the posterior. With the pink shaded region marking the 16–84th percentile range. The stated σ associated with z_{phot} is half of the difference between the upper and lower limits shown above. (Right) Same as the left panels, but for source B.

of $P_{\text{ch,A}} = 7.1 \times 10^{-2}$ and $P_{\text{ch,B}} = 6.9 \times 10^{-2}$ for the two galaxies to be unrelated to FRB 20190614D based on the r -band detections of Galaxies A ($r = 23.24$ mag) and B ($r = 23.93$ mag). The maximum “search radius” r_{ch} used for these estimates take into account the half-light radii $R_{1/2}$ of the host candidates and the distance to the galaxy centroids ($d_{\text{gal,A}} = 2''.22$ and $d_{\text{gal,B}} = 1''.07$) as $r_{\text{ch}} = \sqrt{d_{\text{gal}}^2 + 4R_{1/2}^2}$. We also use the background flux as a limit on the presence of a galaxy below the detection limit of $r > 25.1$ mag. At this limit, the chance association probability of an unrelated galaxy to be located only within the error region of the FRB position is $P_{\text{ch,undet}} = 1.08 \times 10^{-2}$. The probability that source A and source B are unrelated to the FRB is therefore small and the expectation for an even fainter host galaxy counterpart within the error region is even smaller.

We also used the methods of Eftekhari & Berger (2017) to calculate the chance association probabilities.²⁰ Using this approach, we estimate the chance coincidence probabilities of $P_{\text{ch,A}} = 2.6 \times 10^{-2}$ and $P_{\text{ch,B}} = 2.7 \times 10^{-2}$ for Galaxies A and B, respectively. Although, Eftekhari & Berger (2017) followed a similar procedure to Bloom et al. (2002), the estimates using their methods are smaller because they used a more recent estimate of r -band number counts of galaxies (Driver et al. 2016) to calculate the number density of galaxies above any given limiting magnitude. We use the more conservative and more widely used estimates obtained using the formalism of Bloom et al. (2002) to calculate the significance of the FRB candidate.

Under the assumption that an FRB should reside in a galaxy, we can use the host galaxy association to improve the confidence in the significance of the candidate event. The radio signal alone has been characterized by an S/N of 8.27 and an FAR of $4 \times 10^{-3} \text{ hr}^{-1}$. If we assume that false positives are randomly distributed in the field, then the association of the radio source to

a host galaxy improves the confidence in the significance of the FRB candidate as $\text{FAR}_{\text{assoc}} = \text{FAR} \cdot P_{\text{ch,det}}$. According to this relation, we find $\text{FAR}_{\text{assoc}} = 3 \times 10^{-4} \text{ hr}^{-1}$.

Given that the association of a false positive with a host galaxy is unlikely, we conclude that the FRB candidate is an astrophysical event. We used the Transient Name Server²¹ to name the event FRB 20190614D. This naming convention is consistent with a new standard developed by several groups in the FRB community. The common convention used prior to this change is suitable as a shorthand and is “FRB 190614.”

3.2. FRB Host Galaxy and DM

The identification of a specific FRB host galaxy can be critical for both estimating the likely host DM contribution to the total observed DM, and for identifying trends in FRB host galaxy types and environments, which can in turn help discriminate between FRB origin models. FRB 20190614D is offset from optical counterpart(s), the components of which appear to be galaxies that differ in their mass, color, and type.

Given the total extent of the optical counterparts and the color differences, it is most likely that they are two distinct galaxies. However, the photometric redshifts of the two galaxies are consistent with each other and they are close in projection. Assuming a distance of $z = 0.6$ (6.8 kpc/"), the galaxy centers are separated by 13.6 kpc in projection. Assuming that the two galaxies are located at the same redshift, they are likely an interacting pair in which source B may be a star-forming dwarf satellite of source A. If instead we do not assume they are interacting, this projected separation can occur by chance in galaxies of this magnitude about 10% of the time. In this case, one galaxy is the foreground object to the other.

While the optical data do not directly indicate which galaxy might be in the foreground, an analysis of dispersion does provide some hints. The net observed DM is a sum of

²⁰ Implemented in <https://github.com/KshitijAggarwal/casp> (K. Aggarwal et al. 2020, in preparation).

²¹ See <https://wis-tns.weizmann.ac.il/>.

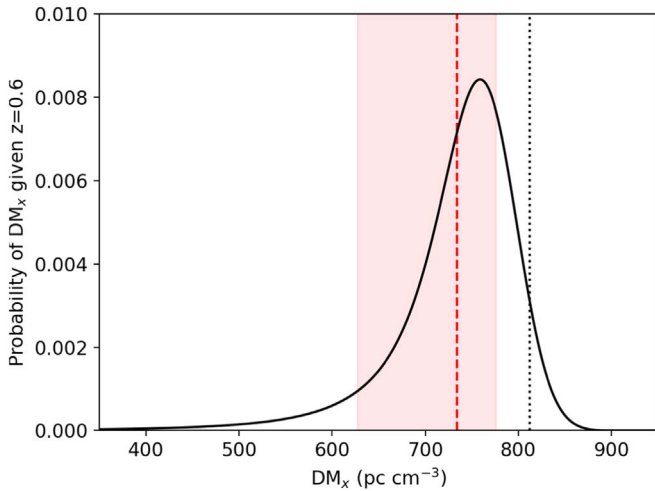


Figure 7. Range of extragalactic DM contributions (predominantly from the IGM and galaxy group halos) predicted by the model of Prochaska & Zheng (2019). The mean and 68% range of the distribution is shown in red. The nominal value of $DM_x = 812 \text{ pc cm}^{-3}$ inferred for FRB 20190614D in Section 3.2 is shown here as a dotted black line.

contributions from the Milky Way’s interstellar medium and its halo, diffuse contributions from IGM plasma, any intervening galaxies and their related circumgalactic media, any cluster plasma, and any host galaxy or FRB-engine contribution (Simha et al. 2020). Any distant contribution is cosmologically redshifted, causing the rest-frame DM contribution to scale by $(1+z)^{-1}$ (e.g., Yao et al. 2017).

Regarding local contributors to DM, for contribution from the interstellar medium of the Milky Way, we adopt the value of 83.5 pc cm^{-3} predicted by Cordes & Lazio (2002). Generally, contributions from the Milky Way’s ionized halo are taken to be $30\text{--}80 \text{ pc cm}^{-3}$; here we adopt the model of Prochaska & Zheng (2019), which predicts a halo contribution of 64 pc cm^{-3} for this sightline. Given these local contributions, we arrive at a representative extragalactic contribution of $DM_x = 812 \pm 25 \text{ pc cm}^{-3}$, which encompasses all nonlocal contributions.

We can use the scaling of DM with redshift (known as the Macquart relation; Macquart et al. 2020) to estimate a maximum possible redshift for our FRB. To do this, we attribute all of DM_x to an IGM that is devoid of cluster and galaxy group halos. There are various models that predict the ionization and elemental make-up of the IGM as a function of redshift; most of these provide results in the same range (e.g., Yao et al. 2017; Pol et al. 2019; Prochaska & Zheng 2019), predicting maximum redshifts in the $z = 1.1\text{--}1.3$ range. These values are well beyond the photometric redshifts we measured for both candidate hosts, implying that there are other significant contributors to DM than the IGM for these sight lines.

Figure 7 shows the expected probability distribution of nonlocal DM components using the model of Prochaska & Zheng (2019). The distribution assumes an FRB located at $z = 0.6$ and uses a parameterized model for halos from individual galaxies, groups, and clusters.²² In this formulation, the mean and 68% range of this distribution gives $DM = 734_{-107}^{+42} \text{ pc cm}^{-3}$. The estimated DM_x for FRB 20190614D is not consistent with the predicted

68% range at this redshift. Note that the peak DM_x probability lies at a higher value than the mean; however, even if we use that as a reference point for indicating potential host contributions, this minimal difference does not change the conclusion or analysis presented below.

There are a few uncertainties in the comparison of measured to expected DM. First, this estimate ignores the host DM, both from the galaxy halo and interstellar medium. Any such component would push the predicted distribution to higher DM, making it more consistent with the observed value. However, this correction term is diminished from the rest-frame value by $1+z_c$, where z_c is the host redshift. For $z = 0.6$, a rest-frame host contribution would be roughly 57 pc cm^{-3} to make the 68% interval of the prediction consistent with the observed value. Second, the DM estimate for the Milky Way tends to be underestimated because the models do not include all small-scale contributions (e.g., $H\alpha$ features) of roughly $\sim 10\text{--}20\%$ of the total DM column. Given this, the predicted DM is marginally consistent with expectations at the best-fit photometric redshift. This tension could be resolved if the FRB host galaxy were more distant than the second, nonhost galaxy of the pair.

While the above constraints do not provide conclusions about which of the two sources the FRB is likely associated with (either galaxy or an interacting pair could provide sufficient host DM contribution), it is worth making the simple note that the FRB’s location appears to be closer in projection to source B, which we found to have a likely bluer stellar component and potentially more star formation. Potential links with star-forming regions in galaxies have been noted for several past FRBs, particularly the localized repeating FRBs (e.g., Tendulkar et al. 2017; Prochaska et al. 2019b; Marcote et al. 2020).

4. Conclusions

We present the discovery of FRB 20190614D by VLA/*realfast*, the first FRB discovered blindly via interferometric imaging. The *realfast* system has a relatively high sensitivity and localization precision, which makes it possible to identify distant FRBs and associate them to host galaxies. We describe how the use of interferometric images enable simultaneous noise estimates that are more robust than the traditional time-local noise estimates. The radio event significance is low, but we argue that the nature of the radio measurement, considered with its association to a pair of host galaxies, is consistent with an astrophysical origin.

FRB 20190614D has the highest DM of any well-localized FRB ($DM_x \approx 812 \text{ pc cm}^{-3}$) and is likely associated with a pair of host galaxies that are among the most distant hosts identified ($z \sim 0.6$). At this distance, the burst energy is $\sim 10^{31} \text{ erg Hz}^{-1}$; the fluence, distance, and energy make this a faint version of the population typically seen by the Parkes Observatory (Shannon et al. 2018).

The DM is somewhat larger than predicted at the distance of the host galaxies, which implies a modest contribution from the FRB environment or intervening galaxy. The two associated galaxies differ in their colors and stellar masses, which implies different environments for the FRB. However, they are broadly consistent with Milky Way–like stellar masses and star formation rates, as has been identified in other FRB associations (Bhandari et al. 2020).

²² Model implemented in Prochaska et al. (2019) with cosmological parameters described in Planck Collaboration et al. (2016).

The *realfast* system continues to commensally search for FRBs and other fast transients during VLA observations. In the future, the system will transition to a community service mode, in which real-time alerts are distributed automatically.

We thank the CHIME collaboration for supporting the analysis for this FRB and the NRAO for supporting *realfast* development and operations. We recognize and acknowledge the very significant cultural role and reverence that the summit of Maunakea has always had within the indigenous Hawaiian community. We are most fortunate to have the opportunity to conduct observations from this mountain.

C.J.L. acknowledges support under NSF grant 2022546. B.Z. acknowledges the support of Frank and Peggy Taplin Membership Fund. On behalf of the F⁴ team, J.X.P., A.M., N.T., K.E.H., and S.S. acknowledge support under NSF grants AST-1911140 and AST-1910471. S.B.S. and K.A. acknowledge support by NSF grant 1714897. S.B.S. is a CIFAR Azrieli Global Scholar in the Gravity and the Extreme Universe program. N.T. acknowledges support by FONDECYT grant 11191217. The NANOGrav project receives support from National Science Foundation (NSF) Physics Frontier Center award number 1430284. P.C. is supported by an FRQNT Doctoral Research Award.

The National Radio Astronomy Observatory is a facility of the National Science Foundation operated under cooperative agreement by Associated Universities, Inc. Part of this research was carried out at the Jet Propulsion Laboratory, California Institute of Technology, under a contract with the National Aeronautics and Space Administration. The Pan-STARRS1 Surveys (PS1) and the PS1 public science archive have been made possible through contributions by the Institute for Astronomy, the University of Hawaii, the Pan-STARRS Project Office, the Max-Planck Society and its participating institutes, the Max Planck Institute for Astronomy, Heidelberg and the Max Planck Institute for Extraterrestrial Physics, Garching, The Johns Hopkins University, Durham University, the University of Edinburgh, the Queen's University Belfast, the Harvard-Smithsonian Center for Astrophysics, the Las Cumbres Observatory Global Telescope Network Incorporated, the National Central University of Taiwan, the Space Telescope Science Institute, the National Aeronautics and Space Administration under grant No. NNX08AR22G issued through the Planetary Science Division of the NASA Science Mission Directorate, the National Science Foundation grant No. AST-1238877, the University of Maryland, Eotvos Lorand University (ELTE), the Los Alamos National Laboratory, and the Gordon and Betty Moore Foundation. Some/all of the data presented in this paper were obtained from the Mikulski Archive for Space Telescopes (MAST). STScI is operated by the Association of Universities for Research in Astronomy, Inc., under NASA contract NAS5-26555. Support for MAST for non-HST data is provided by the NASA Office of Space Science via grant NNX13AC07G and by other grants and contracts. This research has made use of NASAs Astrophysics Data System.

Based on observations obtained at the international Gemini Observatory, a program of NSF's OIR Lab, which is managed by the Association of Universities for Research in Astronomy (AURA) under a cooperative agreement with the National Science Foundation, on behalf of the Gemini Observatory partnership: the National Science Foundation (United States),

National Research Council (Canada), Agencia Nacional de Investigación y Desarrollo (Chile), Ministerio de Ciencia, Tecnología e Innovación (Argentina), Ministério da Ciência, Tecnologia, Inovações e Comunicações (Brazil), and Korea Astronomy and Space Science Institute (Republic of Korea). The Gemini GMOS and NIRI data were obtained from programs GN-2019A-Q-107 and GN-2020A-FT-201 (PI Spolaor), respectively, and it were processed using the Gemini's PYRAF and DRAGONS packages,²³ respectively.

Data were obtained at the W. M. Keck Observatory, which is operated as a scientific partnership among Caltech, the University of California, and the National Aeronautics and Space Administration (NASA). The Keck Observatory was made possible by the generous financial support of the W. M. Keck Foundation.

Facilities: EVLA, Pan-STARRS, MAST, Keck, Gemini, NOT.

Software: rfpipeline (Law 2017), astropy (Astropy Collaboration et al. 2013; Price-Whelan et al. 2018), aegean (Hancock et al. 2018), DRAGONS, pypeit (Prochaska et al. 2019a), (Prochaska et al. 2019).

Appendix

Robust Estimate of Event Significance with Interferometric Images

We describe the detection of an event with an S/N estimate on the border between statistically significant and not. Therefore, we have to be very careful about assessing both its power and the expected noise floor. A small change in the noise standard deviation estimate (and therefore the S/N) will dramatically change its probability of chance occurrence. This type of error, though rarely considered, can push the detection threshold for FRBs and pulsars up by as much as 10% in typical radio time-domain surveys. Correcting this type of error was shown to provide a substantial sensitivity improvement when applied to gravitational wave data in Zackay et al. (2019).

The S/N is derived from a detection score that is a particular linear combination of the data:

$$S(\alpha, \delta) = \sum_{f,i,j,p} G(i, j) V_{f,i,j,p} e^{i\phi_{f,i,j}(\alpha, \delta)}, \quad (\text{A1})$$

where $V_{f,i,j,p}$ are the visibilities of antennae i, j at frequency f and polarization p , $G_{i,j}$ are the empirically measured gains and ϕ are the calculated phases using the position α, δ . To a very good approximation, under the noise hypothesis and assuming no significant RFI, the score follows a Gaussian distribution. The tail of the Gaussian distribution is approximately proportional to

$$P(S > x) \propto e^{-x^2/2}. \quad (\text{A2})$$

For a Gaussian distribution, a 5% change in the noise estimate translates to a factor of 30 in the chance occurrence probability of a tail event above a threshold of S/N = 8. We therefore must have a noise standard deviation estimate that is good to $\approx 1\%$, which has less than a factor of two uncertainty in the chance occurrence probability. Empirically obtaining a 1% estimate of the noise standard deviation requires of order 2×10^4 independent measurements to average over.

Obtaining such an accurate estimate is nontrivial in general. A common approach is to produce a time series of detection

²³ <https://www.gemini.edu/sciops/data-and-results/processing-software/>

scores at a single direction in the sky (either a single-dish beam or phased array of an interferometer), and computing a running standard deviation to use. However, in order to obtain 10^4 independent samples, a few seconds of data are required, and slow gain fluctuations would typically bias the measurement. Our case was further complicated by the fact that the candidate FRB was discovered while the *realfast* system was turning on, so the number of recorded visibilities changes as a function of frequency/baseline/time. This precludes simple local noise estimates based on neighboring time or frequency samples.

We chose to use the image standard deviation as our noise estimate. To provide justification for using this estimate and to assess its biases, we think of the phases in Equation (A1) as random, uncorrelated variables with uniform distribution in $[0, 2\pi]$. From symmetry arguments, this standard deviation would depend only on the sum of the squared visibility amplitudes, or the total momentary power registered by all antennae.²⁴ Since the FRB contributes $\ll 1\%$ of the total power, it can be ignored. Therefore, the relative statistical error in the standard deviation is proportional to the inverse square root of the numbers of visibilities, which is smaller than 1%.²⁵

We also note that if the empirically measured complex gains are accurate to 10%, the S/N estimate we produce would be accurate to within 1% of the optimal S/N with exact gains as the first-order effect of gain errors (or FRB spectral shape) would cancel. See Zackay et al. (2019) for a detailed computation on a similar problem for the case of detecting gravitational waves.

ORCID iDs

Casey J. Law  <https://orcid.org/0000-0002-4119-9963>
 Bryan J. Butler  <https://orcid.org/0000-0002-5344-820X>
 J. Xavier Prochaska  <https://orcid.org/0000-0002-7738-6875>
 Barak Zackay  <https://orcid.org/0000-0001-5162-9501>
 Sarah Burke-Spolaor  <https://orcid.org/0000-0003-4052-7838>
 Nicolas Tejos  <https://orcid.org/0000-0002-1883-4252>
 Alexander Josephy  <https://orcid.org/0000-0003-3059-6223>
 Bridget Andersen  <https://orcid.org/0000-0001-5908-3152>
 Pragya Chawla  <https://orcid.org/0000-0002-3426-7606>
 Kasper E. Heintz  <https://orcid.org/0000-0002-9389-7413>
 Kshitij Aggarwal  <https://orcid.org/0000-0002-2059-0525>
 Geoffrey C. Bower  <https://orcid.org/0000-0003-4056-9982>
 Paul B. Demorest  <https://orcid.org/0000-0002-6664-965X>
 Justin Linford  <https://orcid.org/0000-0002-3873-5497>
 Ryan Mckinven  <https://orcid.org/0000-0001-7348-6900>
 Shriharsh Tendulkar  <https://orcid.org/0000-0003-2548-2926>
 Sunil Simha  <https://orcid.org/0000-0003-3801-1496>

References

Agarwal, D., Aggarwal, K., Burke-Spolaor, S., Lorimer, D. R., & Garver-Daniels, N. 2020, *MNRAS*, **497**, 1661
 Astropy Collaboration, Robitaille, T. P., Tollerud, E. J., et al. 2013, *A&A*, **558**, A33
 Bannister, K. W., Deller, A. T., Phillips, C., et al. 2019, *Sci*, **365**, 565
 Bassa, C. G., Tendulkar, S. P., Adams, E. A. K., et al. 2017, *ApJL*, **843**, L8
 Becker, R. H., White, R. L., & Helfand, D. J. 1995, *ApJ*, **450**, 559

Bertin, E., Mellier, Y., Radovich, M., et al. 2002, in ASP Conf. Ser. 281, The TERAPIX Pipeline, ed. D. A. Bohlender, D. Durand, & T. H. Handley (San Francisco, CA: ASP), 228
 Bhandari, S., Sadler, E. M., Prochaska, J. X., et al. 2020, *ApJ*, **895**, 37
 Bloom, J. S., Kulkarni, S. R., & Djorgovski, S. G. 2002, *AJ*, **123**, 1111
 Brammer, G. B., van Dokkum, P. G., & Coppi, P. 2008, *ApJ*, **686**, 1503
 Burke-Spolaor, S., Bailes, M., Johnston, S., et al. 2011, *MNRAS*, **416**, 2465
 Caleb, M., Stappers, B., Barr, E., et al. 2019, *ATel*, **13098**, 1
 Calzetti, D., Armus, L., Bohlin, R. C., et al. 2000, *ApJ*, **533**, 682
 Chambers, K. C., Magnier, E. A., Metcalfe, N., et al. 2016, arXiv:1612.05560
 Champion, D. J., Petroff, E., Kramer, M., et al. 2016, *MNRAS*, **460**, L30
 Chatterjee, S., Law, C. J., Wharton, R. S., et al. 2017, *Natur*, **541**, 58
 CHIME/FRB Collaboration, Amiri, M., Bandura, K., et al. 2018, *ApJ*, **863**, 48
 CHIME/FRB Collaboration, Amiri, M., Bandura, K., et al. 2019, *Natur*, **566**, 235
 Cordes, J. M., & Chatterjee, S. 2019, *ARA&A*, **57**, 417
 Cordes, J. M., & Lazio, T. J. W. 2002, arXiv:astro-ph/0207156
 Cordes, J. M., Wasserman, I., Hessels, J. W. T., et al. 2017, *ApJ*, **842**, 35
 Cornwell, T., & Fomalont, E. B. 1999, in ASP Conf. Ser. 180, Synthesis Imaging in Radio Astronomy II, ed. G. B. Taylor, C. L. Carilli, & R. A. Perley (San Francisco, CA: ASP), 187
 Driver, S. P., Andrews, S. K., Davies, L. J., et al. 2016, *ApJ*, **827**, 108
 Eftekhari, T., & Berger, E. 2017, *ApJ*, **849**, 162
 Eftekhari, T., Berger, E., Williams, P. K. G., & Blanchard, P. K. 2018, *ApJ*, **860**, 73
 Flewelling, H. A., Magnier, E. A., Chambers, K. C., et al. 2016, arXiv:1612.05243
 Gajjar, V., Siemion, A. P. V., Price, D. C., et al. 2018, *ApJ*, **863**, 2
 Ginzburg, V. L. 1973, *Natur*, **246**, 415
 Greisen, E. W. 2003, in Astrophysics and Space Science Library, Vol. 285, AIPS, the VLA, and the VLBA, ed. A. Heck (Dordrecht: Kluwer), 109
 Hancock, P. J., Trott, C. M., & Hurlley-Walker, N. 2018, *PASA*, **35**, e011
 Hodapp, K. W., Jensen, J. B., Irwin, E. M., et al. 2003, *PASP*, **115**, 1388
 Inoue, S. 2004, *MNRAS*, **348**, 999
 Josephy, A., Chawla, P., Fonseca, E., et al. 2019, *ApJL*, **882**, L18
 Kocz, J., Ravi, V., Catha, M., et al. 2019, *MNRAS*, **489**, 919
 Law, C. J. 2017, rfpipeline: Radio Interferometric Transient Search Pipeline, Astrophysics Source Code Library, ascl:1710.002
 Law, C. J., Abruzzo, M. W., Bassa, C. G., et al. 2017, *ApJ*, **850**, 76
 Law, C. J., Bower, G. C., Burke-Spolaor, S., et al. 2018, *ApJS*, **236**, 8
 Lawrence, E., Vander Wiel, S., Law, C., Burke Spolaor, S., & Bower, G. C. 2017, *AJ*, **154**, 117
 Lorimer, D. R., Bailes, M., McLaughlin, M. A., Narkevic, D. J., & Crawford, F. 2007, *Sci*, **318**, 777
 Lu, W., & Kumar, P. 2016, *MNRAS*, **461**, L122
 Macquart, J. P., Prochaska, J. X., McQuinn, M., et al. 2020, *Natur*, **581**, 391
 Marcote, B., Nimmo, K., Hessels, J. W. T., et al. 2020, *Natur*, **577**, 190
 Marcote, B., Paragi, Z., Hessels, J. W. T., et al. 2017, *ApJL*, **834**, L8
 Masui, K., Lin, H.-H., Sievers, J., et al. 2015, *Natur*, **528**, 523
 McMullin, J. P., Waters, B., Schiebel, D., Young, W., & Golap, K. 2007, in Astronomical Society of the Pacific Conference Series, Vol. 376, Astronomical Data Analysis Software and Systems XVI, ed. R. A. Shaw, F. Hill, & D. J. Bell, 127
 Noll, S., Burgarella, D., Giovannoli, E., et al. 2009, *A&A*, **507**, 1793
 Oostrum, L. C., van Leeuwen, J., Attema, J., et al. 2017, *ATel*, 10693, 1
 Perley, R. A., & Butler, B. J. 2017, *ApJS*, **230**, 7
 Perley, R. 2016, Jansky Very Large Array Primary Beam Characteristics, NRAO, EVLA Memo 195
 Petroff, E., Hessels, J. W. T., & Lorimer, D. R. 2019, *A&ARv*, **27**, 4
 Planck Collaboration, Ade, P. A. R., Aghanim, N., et al. 2016, *A&A*, **594**, A13
 Pokorny, M., Law, C. J., Bower, G. C., et al. 2018, *JAI*, **7**, 1850005
 Pol, N., Lam, M. T., McLaughlin, M. A., Lazio, T. J. W., & Cordes, J. M. 2019, *ApJ*, **886**, 135
 Price-Whelan, A. M., Sipőcz, B. M., Günther, H. M., et al. 2018, *AJ*, **156**, 123
 Prochaska, J. X., Hennawi, J., Cooke, R., et al. 2019a, PyPEIT: Python Spectroscopic Data Reduction Pipeline, ascl:1911.004
 Prochaska, J. X., Macquart, J.-P., McQuinn, M., et al. 2019b, *Sci*, **366**, 231
 Prochaska, J. X., Simha, S., Law, C., & Tejos, N. 2019, FRBs/FRB: First DOI Release of this Repository v1.0.0, Zenodo, doi:10.5281/zenodo.3403651
 Prochaska, J. X., & Zheng, Y. 2019, *MNRAS*, **485**, 648
 Ravi, V. 2019a, *NatAs*, **3**, 928
 Ravi, V. 2019b, *ApJ*, **872**, 88
 Ravi, V., Catha, M., D'Addario, L., et al. 2019, *Natur*, **572**, 352
 Rest, A., Stubbs, C., Becker, A. C., et al. 2005, *ApJ*, **634**, 1103
 Schechter, P. L., Mateo, M., & Saha, A. 1993, *PASP*, **105**, 1342

²⁴ According to Parseval's theorem, the standard deviation of the image is exactly equal to the standard deviation estimate using the absolute value squared of the visibilities.

²⁵ $N_{\text{vis}} = N_{\text{bl}} * N_{\text{ch}} * N_{\text{pol}} * f_{\text{recorded}} = 351 * 166 * 2 * 0.38 = 4.5e4$.

- Shannon, R. M., Macquart, J. P., Bannister, K. W., et al. 2018, *Natur*, **562**, 386
- Simha, S., Burchett, J. N., Prochaska, J. X., et al. 2020, arXiv:2005.13157
- Spitler, L. G., Cordes, J. M., Hessels, J. W. T., et al. 2014, *ApJ*, **790**, 101
- Spitler, L. G., Scholz, P., Hessels, J. W. T., et al. 2016, *Natur*, **531**, 202
- Tendulkar, S. P., Bassa, C. G., Cordes, J. M., et al. 2017, *ApJL*, **834**, L7
- The CHIME/FRB Collaboration, Andersen, B. C., Bandura, K., et al. 2019, *ApJ*, **885**, 24
- Thornton, D., Stappers, B., Bailes, M., et al. 2013, *Sci*, **341**, 53
- Tonry, J. L., Stubbs, C. W., Lykke, K. R., et al. 2012, *ApJ*, **750**, 99
- Vedantham, H. K., & Ravi, V. 2019, *MNRAS*, **485**, L78
- Yao, J. M., Manchester, R. N., & Wang, N. 2017, *ApJ*, **835**, 29
- Zackay, B., Venumadhav, T., Roulet, J., Dai, L., & Zaldarriaga, M. 2019, arXiv:1908.05644
- Zhang, Y. G., Gajjar, V., Foster, G., et al. 2018, *ApJ*, **866**, 149